J. Biophotonics **9**, No. 5, 499–509 (2016) / **DOI** 10.1002/jbio.201500203

Journal of BIOPHOTONICS

FULL ARTICLE

Hybrid method of strain estimation in optical coherence elastography using combined sub-wavelength phase measurements and supra-pixel displacement tracking

Vladimir Y. Zaitsev[*, 1, 2, 3], *Alexander L. Matveyev*[1, 2], *Lev A. Matveev*[1, 2], *Grigory V. Gelikonov*[1, 2], *Ekaterina V. Gubarkova*[2], *Natalia D. Gladkova*[2], *and Alex Vitkin*[2, 4]

[1] Institute of Applied Physics of the Russian Academy of Sciences, 46 Uljanova St., 603950, Nizhny Novgorod
[2] State Medical Academy of Nizhny Novgorod; 1 Minina Square, 10/1 Minina Square, Nizhny Novgorod 603005, Russia
[3] State University of Nizhny Novgorod, 23 Gagarina avenue, 603950, Nizhny Novgorod, Russia
[4] University of Toronto, Toronto, Canada

Received 30 July 2015, revised 10 October 2015, accepted 12 October 2015
Published online 14 November 2015

Key words: Optical coherence elastography, strain mapping, displacement tracking, phase-resolved OCT

A novel hybrid method which combines sub-wavelength-scale phase measurements and pixel-scale displacement tracking for robust strain mapping in compressional optical coherence elastography is proposed. Unlike majority of OCE methods it does not rely on initial reconstruction of displacements and does not suffer from the phase-wrapping problem for super-wavelength displacements. Its robustness is enabled by direct fitting of local phase gradients obviating the necessity of phase unwrapping and error-prone numerical differentiation. Furthermore, axial displacements significantly exceeding not only the optical wavelength, but pixel scales (i.e., multiple wavelengths) can be efficiently tracked and compensated. This feature strongly reduces errors in phase-gradient estimation and ensures high robustness with respect to both additive and decorrelation noises.

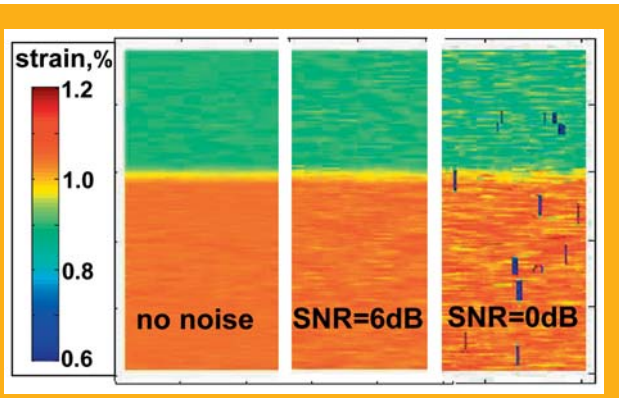

Illustration of exceptionally high tolerance of the proposed method to noises: contrast of only 25% in the stiffness of the layers is clearly seen in the strain map even for equal intensities of the OCT signal and additive noise (SNR = 0 dB).

1. Introduction

Elastographic mapping in OCT has attracted much attention since seminal works of Schmitt [1], where the so-called compressional elastography was proposed based on correlational speckle tracking. The key assumption in the compression approach is that approximately uniform uniaxial stress field is created in the vicinity of a rigid OCT probe pressed onto the surface of the studied tissue. Consequently the distribution of strains in this region can be used to map out stiffness distribution, because stiffer regions

* Corresponding author: e-mail: vyuzai@mail.ru

should be less deformed. It is usually implicitly assumed that the initial displacement field should be reconstructed and then differentiated to extract local strains. A significant portion of such studies were based on utilization of correlational tracking of displacements [2–4]. More advanced variants of this approach were developed recently [5–8], in particular progressing from correlational processing of intensity-only images to making use of complex-valued signals.

In parallel, significant attention has been paid to approaches in which the displacement-field reconstruction is based on phase-resolved measurements [9, 10]. Further, elastographic OCT approaches which do not rely on the initial displacement-field reconstruction were also proposed (in particular, direct exploitation of strain-induced decorrelation of OCT scans [11, 12] or methods based of direct measurement of velocities of surface of shear waves [13]. However, the use of compression-produced displacements and strains for elastographic mapping continues to attract significant attention, due to simplicity of the basic idea and prospects of developing a free-hand practical device using the OCT probe itself as the compression source.

Assessment of correlational approaches to speckle tracking presented in recent works [7, 14, 15] indicates that correlational methods of displacement tracking, while fairly successful in mechanical engineering applications (based on processing of digital photographic images), are significantly corrupted by speckle-blinking effects intrinsic to OCT. To overcome this, super-broadband (almost white-light) OCT sources or very large-scale signal processing correlation windows are needed to ensure reasonable accuracy and strain sensitivity. However, the former is technologically and practically challenging, while the latter strongly reduces the resultant resolution of the stain maps, often down to levels unacceptable in practice.

During the last decade, phase-resolved methods have gradually become dominant in compression-based approaches, in part due to their intrinsically higher sensitivity to displacements [10, 16–18] and better tolerance to strain-induced speckle blinking (e.g., see discussions in [14, 15]). Detailed discussions of the various aspects of strain estimation by OCT phase methods can be found in recent works [10, 16].

Let us briefly review the pros and cons of the two OCE approaches. (i) Phase-resolved methods enable significantly higher accuracy of displacement measurements compared to correlational tracking. The reason is that in the latter methods, the measurement error is determined by the OCT image pixel size scale (typically ~5–10 μm), i.e., a value significantly greater than one wavelength (typically ~1 μm). In contrast, in phase methods the error is on the order of a fraction of one wavelength. (ii) Measuring displacements on the order of several pixels (i.e. ~tens of microns) is readily feasible via correlational procedures, whereas in phase-resolved methods, the much higher (sub-wavelength) sensitivity is coupled with a much lower range of displacements that can be unambiguously measured. This arises because of the 2π periodicity of phase (the corresponding ambiguity can potentially be addressed by phase unwrapping if the phase varies in steps smaller than 2π) [10, 19]; thus, for OCT scans formed by backscattered light, the displacements directly measured via phase variations (without phase unwrapping) are limited to $\lambda_0/2 \sim 0.5$ μm, where λ_0 is the central wavelength of the OCT source. Since typical depth of OCT image is 1–2 mm (~10^3 μm), only strains smaller than ~10^{-3} allow for unambiguous phase-based direct measurement of displacements. If phase unwrapping procedures are applied to incrementally increasing displacement to remedy this limitation, the accumulated displacement can exceed $\lambda_0/2$. Further, in the presence of additional noises, the unwrapping procedure can yield phase-breaking errors of $\pm\pi$ rad, which are not corrected at subsequent steps and lead to corresponding breaks in the reconstructed displacements. Clearly then, combining the relative advantages/limitations of the correlation-tracking and phase-based approaches may prove useful for improving OCE performance.

In what follows we thus propose a hybrid approach in which phase measurements are combined with elements of pixel-scale displacement tracking (hybrid phase-resolved/displacement-tracking (HPRDT) method). Note that this is not a straightforward "addition" of correlational speckle-tracking procedures and conventional phase measurements of displacements, as will be detailed below. A particularly noteworthy feature is that although HPRDT is able to reconstruct axial displacements over the entire OCT scan, this reconstruction is not essential for strain mapping *per se*. That is, HPRDT method estimates local strains by comparing reference and deformed OCT scans, *without* the initial reconstruction of the displacement field and subsequent error-prone procedure of numerical differentiation. The application of the proposed approach makes it possible to significantly extend the range of strains and displacements within its range of validity. Further, HPRDT is seen to be robust in the context of additive noises, compared to conventional correlation-tracking and phase-resolved methods, as demonstrated in the following sections.

2. Methodology: HPRDT performance compared to conventional approaches

The main goal of compression elastography is reconstruction of local strains rather than displacements

of scatterers in the compressed tissue. For determining strain over a chosen region (we call this region "window" by analogy to the correlation window used in correlational image processing), one needs to know the difference in displacements over the window scale. In the simplest case, this leads to the following finite-difference approximation of the axial strain s:

$$s = \frac{d_2 - d_1}{z_2 - z_1} = \frac{\Delta d}{\Delta z} \tag{1}$$

where $\Delta z = z_2 - z_1$ is the axial dimension of the chosen window (differentiation scale) and $\Delta d = d_2 - d_1$ is the difference in the displacements of particles located at the extremes of the window. In phase methods, the displacement d is related to the phase variation $\delta\varphi$ of the OCT signal and the central wavelength λ_0 as [10]

$$d = \frac{\lambda_0 \cdot \delta\varphi}{4\pi n} \tag{2}$$

where n is the refractive index of the tissue. Because of 2π periodicity of the phase, displacements exceeding half-wavelength cannot be directly determined unambiguously, but only within an uncertainty proportional to integer numbers of $\lambda_0/2$.

Since in a strained tissue, the displacement d is proportional to the average strain s and depth z counted from the OCT-probe surface ($d \approx s \cdot z$ from Eq. (1)), for the depth range $\sim 10^2 - 10^3$ μm, displacements and phase variations are unambiguously related over the entire depth only for strains smaller than $\sim 10^{-3} - 10^{-4}$. For larger strains or depths, noise-sensitive phase unwrapping procedures are required. However, for estimating strains (i.e., gradients of the displacement field), one does not need to know *entire displacements* at all. Rather, one needs to determine the *difference in displacements* over the chosen scale $\Delta z = z_2 - z_1$. Therefore, the same unknown ambiguity in the total displacements d_1 and d_2 does not prevent correct evaluation of strain over the scale Δz, unless the difference in the displacements $\Delta d \approx s \cdot \Delta z$ exceeds $\lambda_0/2$ and the corresponding phase difference Δd acquires additional ambiguity of 2π rad. The resultant limitation on the allowable strain $s \cdot \Delta z < \lambda_0/2$ is much less restricting than for the entire axial depth of OCT imaging, since the scale $\Delta z = z_2 - z_1$ is typically much smaller than the OCT penetration depth. To put in some typical numbers – for pixel dimension $\sim 5 - 10$ μm and a reasonable differentiation scale $\Delta z \sim 10$ pixels (corresponding to the physical size $\Delta z \sim 50 - 100$ μm), the allowable strain may reach $\lambda_0/(2 \cdot \Delta z \cdot n) \sim 10^{-2}$, which is significantly greater than for displacement measurements over the entire OCT imaging depth.

In many practically interesting situations, for example, when the compression is created by a well-controlled piezo-actuator rather than produced by hand [20], the displacement over the entire depth can be limited to several micrometers, ensuring that throughout the entire scan, the difference $d_2 - d_1 < \lambda_0/2$ within the effective differentiation window Δz; thus, for estimating strain, unwrapping is unnecessary despite phase ambiguity over the entire scan. This is diagrammatically illustrated in Figure 1.

Furthermore, even if for larger strains $\Delta d = s \cdot \Delta z$ exceeds $\lambda_0/2$, it is much simpler to apply the unwrapping procedure within the small differentiation window (say once or twice) than attempting to unwrap multiple periods over entire A-scan depth. Besides, potential errors in unwrapping for a particular window position are "local", in that they do not affect strain estimation above or below it.

Next, having a set of a ~dozen points of the depth-dependence of the phase variations within the window, we do not employ the rather unstable finite-difference strain estimation via Eq. (1); instead, much stabler results are obtained by fitting the phase gradient within the window, for example, applying a least-square procedure. Similar advantage of strain estimation via least-square fitting of the displacement gradient in comparison with the straightforward differentiation of displacement via finite-difference derivative estimation was discussed in [10]. In that paper, applying a weighted least-square fitting that accounts for signal-to-noise ratio within the size of the window chosen for strain estimation was shown to be advantageous. Analogously here, we propose to estimate the axial gradient of phase variations over a rectangular window rather than along individual A-scans. In such a case, estimation of

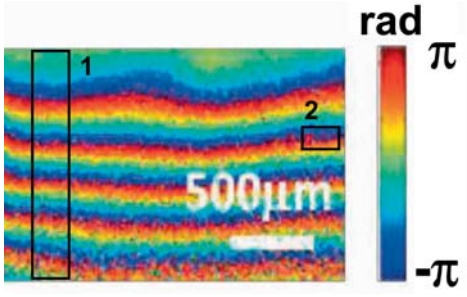

Figure 1 Color-encoded phase difference between a reference B-scan and axially deformed one, illustrating the phase-variation ambiguity of many periods over the entire depth (window 1) and absence of such ambiguity within a smaller window 2, which is sufficient for locally estimating strain via the phase gradient. Displacement-induced decorrelation noise is clearly seen in the deeper regions that experience larger displacements significantly exceeding the wavelength.

phase variations with proper accounting for varying pixel amplitudes can be efficiently accomplished via the Kasai phase estimator [21], with averaging in the lateral direction over the strain-estimation window.

Namely, for the analysis window with the size M px in the vertical and N px in horizontal directions, the phase difference for the compared B-scans is calculated for a given position of the window center for every j-th row within the window with averaging over its horizontal size. If one introduces the complex-valued amplitude $A = |A| \exp(\mathrm{i}\varphi)$ of each pixel and the notations $Q = \mathrm{Re}(A)$ and $I = \mathrm{Im}(A)$ for the cosine and sine quadrature components, the corresponding Kasai estimate for B-scans with numbers $n+1$ and n can be written in the following form

$$\Delta\varphi(j) = \arctan\left\{\frac{\sum_{k=1}^{N}\left(I_{k,j}^{(n+1)}Q_{k,j}^{(n)} - Q_{k,j}^{(n+1)}I_{k,j}^{(n)}\right)}{\sum_{k=1}^{N}\left(Q_{k,j}^{(n+1)}Q_{k,j}^{(n)} + I_{k,j}^{(n+1)}I_{k,j}^{(n)}\right)}\right\} \qquad (3)$$

Here, for a given position of the analysis window, index j corresponds to the current depth and the averaging index k varies within the horizontal size of the window in the range $[1, N]$.

It is known that an important issue in strain estimation by phase measurements is the problem of gradual degradation of the phase-difference (see the lower part of Figure 1) because of the displacement-induced decorrelation [16]. The origin of such "decorrelation noise" is physically clear. Indeed, if one compares a pixel in the reference B-scan with the pixel having the same coordinates in the displaced image, the scatterers initially localized in the reference pixel can already be displaced towards another pixel and replaced (at least partially) by other scatterers with noticeably different initial coordinates and, correspondingly, different initial phase of the scattered signal. Therefore, the phases of the compared signals for pixels with the same coordinates may relate (at least partially) to *different* scatterers, so that the difference of such phases can be random, i.e., unrelated to genuine displacements of the scatterers. Such "decorrelation noise" in real conditions certainly can be accompanied by other additive measurement noises.

Generally speaking, for a given level of noise at the signal receiver, one might expect that if larger strains produce larger phase variations, the latter apparently can be easier measured and can potentially lead to higher signal-to-noise ratio (SNR) thus improving the accuracy. However, for larger strain and larger observation depth, the gradually accumulated displacements can exceed not only the wavelength, but also the pixel size. Such scatterer displacements that are comparable with and exceeding the pixel size can strongly degrade the fidelity of deduced phase variations by the above-elucidated reasons (phase map in Figure 1 gives an example of such degradation at larger depths). Thus, to realize the potential advantage of measuring larger phase gradients, this deleterious effect of displacement-induced decorrelation noise should be overcome. This can be achieved by shifting the strongly displaced fragments of compared images by the (correctly determined) integer number of pixels. Such displacement compensation would enable phase comparison corresponding to the *same scatterers* in the reference and deformed images, instead of (as commonly done) comparing pixels with the same coordinates that might correspond to different scatterers with absolutely unrelated phases. However, it has been verified that straightforward correlational tracking of displacements with an integer-pixel accuracy does not lead to better results and may even introduce additional errors in low SNR regions. This makes intuitive sense because deeper regions of larger displacements to be tracked are indeed the very regions with low SNR.

To overcome this difficulty in pixel-scale displacement compensation, we apply an alternate approach. The values of phase gradients $\Delta\varphi_i$ rad/px determined at smaller depths can be summed to find the accumulated (unwrapped) phase variation for the n-th pixel:

$$\Delta\varphi_{\mathrm{total}}(n) = \sum_{i=1}^{n}\Delta\varphi_i \qquad (4)$$

The so-accumulated phase can be easily transformed into displacement via Eq. (2), so that it is possible to detect the pixel depth (pixel number), for which the total displacement exceeds 0.5 px. Below this threshold value, the phases of the compared fragments of reference and deformed scans can be analyzed directly without a relative mutual shift, whereas for larger depth (and every additional accumulated pixel), the compared fragments can be mutually shifted by the so-found number of pixels. This cumulative displacement tracking and corresponding correction combined with phase measurement strongly reduces the errors caused by displacement-induced decorrelation. As a result, the range of allowable displacements increases up to strain levels for which pronounced speckle blinking occurs, and where conventional correlational and phase-resolved methods of displacement tracking both become inoperable [7, 14, 15]. Figure 2 illustrates the above described measurement steps: (i) determining the phase gradient of the inter-scan phase difference over a chosen window initially in the scan region with sub-pixel displacements; (ii) recalculation of the determined phase gradient into strain; (iii) summation of the previously found phase gradients along the depth coordinate to

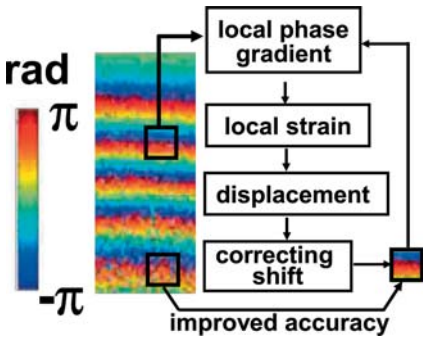

Figure 2 Schematic of strain reconstruction using reconstruction of local phase gradients in a sliding window in combination with cumulative tracking of displacements for reduction of errors due to displacement-induced decorrelation in HPRDT method.

find cumulative displacement for the current depth; (iv) correction of the depth-position of compared pixels (by one pixel if the cumulated displacement for this pixel exceeds 1/2 px, 3/2 px, etc.) for reducing displacement-induced decorrelation noise. It should be emphasized that in regions with significant displacements of scatterers, the so-measured phase variations will be wrapped (that is, it may contain an uncertainty proportional to an integer number of 2π rads as illustrated in Figure 2). Nevertheless, the accuracy of the wrapped phase measured with the scatterer-displacement tracking becomes much higher, as well as the accuracy of the subsequently extracted strains proportional to *local phase gradients* estimated over fairly small scale within the analysis window. For estimating local gradients, an unknown integer number of wrapped phase periods is not critical at all. In the next section, we offer detailed examples illustrating the above-mentioned advantageous features of the proposed HPRDT method.

3. Results and discussion: numerical and experimental examples illustrating the method features

In the numerical simulations, we use the recently developed model [22] to generate and analyze the strain-induced evolution of complex-valued OCT scans. For illustrative purposes and for brevity, we do not consider depth-dependent signal decay and keep the same signal-to-noise ratio throughout the image. Also we do not consider the overlapping of A-scans in the lateral direction (not a principal issue for the discussed problem), so that scatterers in horizontally adjacent pixels are independent. The average density of scatterers is chosen to be 4 per pixel (px). As shown earlier [22], the shape of speckle-intensity histograms stays nearly constant for density of scatterers larger than ~2, in good agreement with properties exhibited by real OCT images. Each A-scan consists of 256 pixels and the total depth of the image is 2048 μm in air. We chose that for depth $z \geq 100$ px, the material is 1.25 times softer than in the upper part, so that the strain in this deeper region is correspondingly 1.25 times greater. The central wavelength of the optical source is chosen 1300 nm and spectral width 100 nm which is a fairly typical value for OCT scanners (and the parameters of the scanner used for experimental demonstrations shown in Figures 7 and 8).

The first example in Figure 3 is given for zero additional noise and demonstrates strain reconstruction using the proposed method in the case of moderate strain (2% in the lower layer and 1.25 times smaller in the upper one). For such strain, the phase-variation ambiguity yet does not occur within the used window size $\Delta z = 10$ px. The displacement increases proportionally to the depth and exceeds 4 px in the deeper part of the image, resulting in many-periods phase ambiguity over the entire depth [see Figure 3(a-1) and (a-2)]. Such displacement produces noticeable decorrelation between the reference and deformed images, as is shown in the correlation map Figure 3(b-1). Correspondingly, the phase-difference map Figure 3(a-1) in the lower part demonstrates significant displacement-induced "decorrelation noise" in the directly-found phase difference between the compared images. Figure 3(c-1) shows the corresponding strain map found via fitting the phase difference between the reference and deformed-tissue images within the chosen window with 10 px vertical and 16 px horizontal size. As discussed in [10], such fitting yields much better results than the finite-difference estimate of strain via Eq. (1); however, for the 2% strain in the considered example, the displacement-induced decorrelation already produces significant errors that strongly corrupt the lower part of strain map [Figure 3(c-1)]. An example of the dependence of strain on the depth found along one vertical slice of Figure 3(c-1) with averaging within the area of the used window 10 px × 16 px in size is shown in the upper panel Figure 3(d-1) and clearly demonstrates gradually increasing strain-estimation error with increasing depth. The lower part of panel (d-1) shows the corresponding depth-dependence of displacement found via accumulation of local phase variations according to Eq. (3). It is seen that in the lower part of the image (where the stain-induced decorrelation strongly corrupts the phase measurements), the so-found displacement strongly deviates from the exact function $d(z)$ used as input to the simulation.

As proposed above, the accumulated displacement can be used for compensation of the displacement-induced decorrelation to improve the strain-estimation accuracy. Namely, when the displacement exceeds 1/2 px, 3/2 px, 5/2 px and so on, we intro-

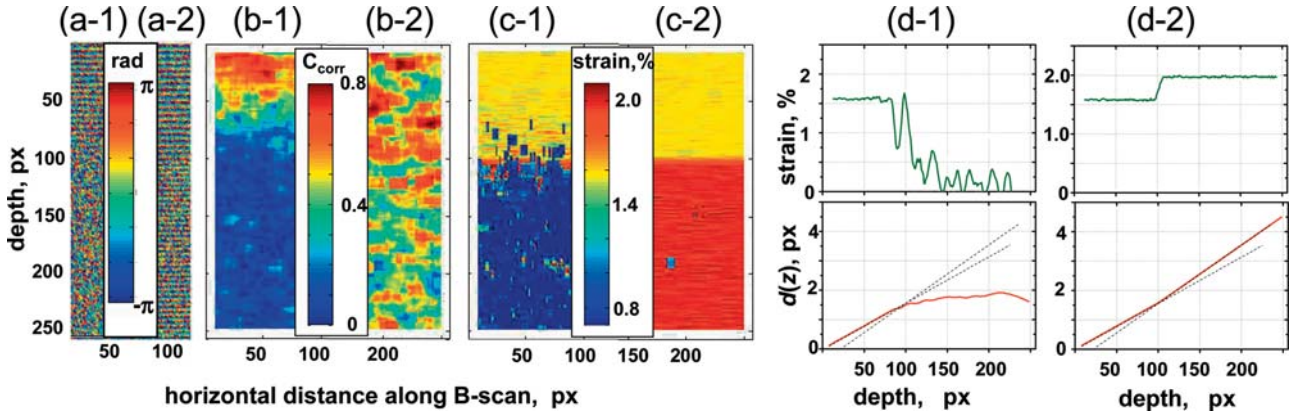

Figure 3 Simulated example of the HPRDT method for reconstructing strains and displacements in the absence of noise. The lower layer is 1.25 times softer (and consequently its strain is 1.25 times greater). Strain in the stiffer upper layer is 2%. For this strain level, there is no phase ambiguity for the chosen size of the window (10 px in vertical and 16 px in the horizontal direction), whereas multiple phase-variation periods occur over the entire depth. Maximum displacement at the image bottom is over 4.5 px. Panels (a-1) and (a-2) are the phase-variation maps found without and with displacement compensation by integer number of pixels, respectively. Panels (b-1) and (b-2) are cross-correlation maps for zero-mean normalized Pearson cross-correlation coefficient [23], C_{corr} between the compared images found without displacement compensation and with compensation, respectively. Panels (c-1) and (c-2) are strain maps found without and with interger-pixel displacement tracking, respectively. Upper panel (d-1) is a single vertical profile (along x = 100 px) of the 2D strain map from panel (c-1) without displacement tracking. Upper panel (d-2) is a similar profile found with displacement tracking, showing significant accuracy improvement. Lower parts of panels (d-1) and (d-2) are the displacements $d(z)$ found via summation of estimated local phase gradients [Eq. (3)]. Dashed lines are guides for the eye showing exact slopes of $d(z)$ used in the simulation. It is clear that in the lower part of the image, where displacements exceed the pixel-scale, the correcting integer-pixel tracking significantly improves the quality of strain and displacement estimation.

duce the corresponding compensating shift by an integer number of pixels (i.e., 1, 2, 3 px and so on) when comparing the phases of the reference and deformed images. Such displacement tracking and the corresponding compensation of pixel-scale displacements makes it possible to significantly increase cross-correlation between the compared scans, as is clear from the correlation coefficient (zero-mean normalized Pearson cross-correlation coefficient, C_{corr} [23]) mapped in Figure 3(b-2) found with the compensation (compare with Figure 3(b-1) without compensation). The phase difference found with the displacement compensation [Figure 3(a-2)] also demonstrates much lower influence of displacement-induced decorrelation and yields the strain map [Figure 3(c-2)] that demonstrate much higher quality than Figure 3(c-1) obtained without compensation. The corresponding vertical profiles for strain and displacement [Figure 3(d-2)] also demonstrate significant improvement compared with the plots in Figure 3(d-1) found without displacement compensation.

We emphasize that in contrast to conventionally discussed approaches (based on either correlational [1] or phase-resolved tracking of displacements [9]), in which initial displacement distribution $d(z)$ is reconstructed and then error-prone numerical differentiation is required for finding local strains, in the HPRDT approach these procedures are reversed. First we estimate *local strains* (within the chosen window size by fitting the phase-variation gradient) and then use the determined strain for estimating displacements and performing pixel-scale compensation if necessary. The displacement $d(z)$ thus obtained looks very smooth, because the random errors in strain estimation are efficiently averaged and cancelled.

In addition to illustration of pure decorrelation effects in Figures 3 and 4 we demonstrate the robustness of the proposed approach in the presence of additive noise. We use the same parameters as in Figure 3, but introduce a fairly strong additive Gaussian noise, for which the average SNR is 6 dB (compare with the usually discussed SNR $\sim$10–15 dB [16]). The regular phase variation found without displacement compensation shown Figure 4(a-1) is considerably noisier than in Figure 3(a-1), where only decorrelation noise is present. Application of the displacement-compensation noticeably improves the phase estimation [Figure 4(a-2)], although the cross-correlation between the compared images remains significantly reduced over the entire scan area (down to $C_{corr} \sim 0.4$), even after application of the displacement-compensation procedure as seen from the correlation maps Figure 4(b-1) and (b-2). Nevertheless, in comparison with Figure 4(c-1) (without displacement compencation) the 2D strain map in Figure 4(c-2) (with compensation) clearly demonstrate the recovery

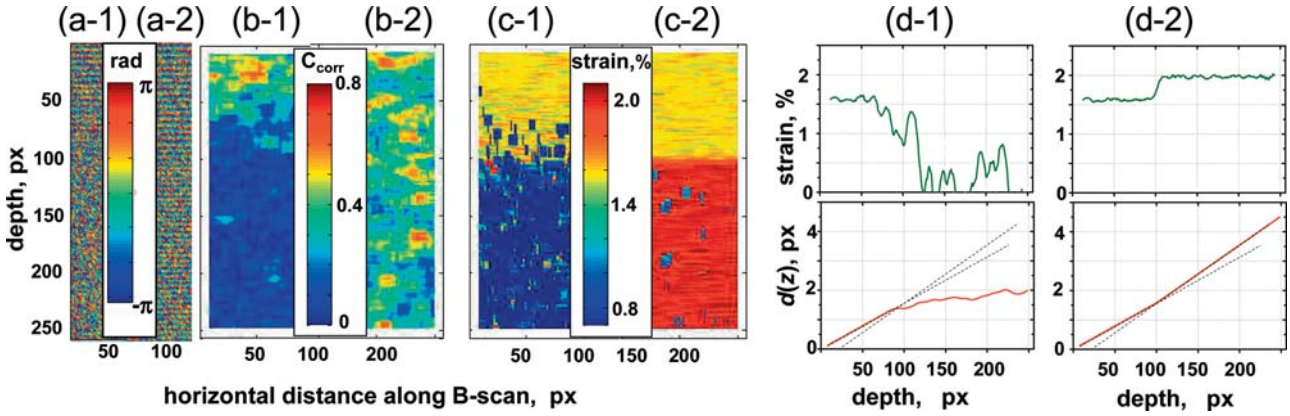

Figure 4 Simulated example of the HPRDT method application for the same parameters as in Figure 3, now in the presence of rather strong Gaussian additive noise with SNR = 6 dB (cf Figure 3). Panels (a-1) and (a-2) are the phase-variation maps and panels (b-1) and (b-2) are cross-correlation maps between the compared images found without and with displacement compensation, respectively. Panels (c-1) and (c-2) are strain maps found without and with displacement tracking, respectively. Upper panel (d-1) is a single vertical profile of the 2D strain map from panel (c-1) without displacement tracking, and significantly more accurate upper panel (c-2) is a similar profile found with displacement tracking. Lower parts of panels (d-1) and (d-2) are the respective depth dependences of the reconstructed displacements $d(z)$. The dotted lines are the guides for the eye showing exact slopes for $d(z)$ used in the simulation.

of the correct contrast in strain value of 1.25X, with quality comparable to the noiseless maps [Figure 3(c-1) and (c-2)]. The quality of upper plot Figure 4(d-2) showing the depth profile of strain and the lower in Figure 4(d-2) for the displacement obtained with displacement compensation still recover excellent results, in fact comparable with the noiseless ones in Figure 3(d-2), despite the fact that SNR is only 6 dB.

Concerning the efficiency of the pixel-scale displacement compensation demonstrated in Figures 3 and 4, one could argue that such compensation would not be necessary at all if the average strain is chosen sufficiently small, say closer to $10^{-4}-10^{-3}$ levels as traditionally considered for phase-resolved methods (see, e.g., [16]). In such a case, the displacement over the entire image remains in the subpixel range (although may exceed the wavelength in certain regions of the OCT scan), so that the displacement-induced decorrelation effects are not so strong. However, note that in such a case the strain-induced variations in the *phase gradient* also become significantly smaller and thus are much harder to detect in the presence of noise. To illustrate this, Figure 5 shows the simulation results for strain = 0.1%, which is still fairly strong for conventionally discussed phase-resolved methods of strain estimation [10, 16], but an order of magnitude smaller than considered in Figures 3 and 4. In such a case, pixel-scale displacement compensation in unnecessary and the HPRDT method in fact becomes equivalent to conventional phase-resolved methods. Figure 5(a-1), (a-2) and (a-3) show the phase difference between the reference and deformed images for different levels of noise. Slight irregularities in the noiseless Figure 5(a-1) are entirely due to weak decorrelation effects. In Figure 5(a-2) and (a-3), the phase-measurement errors are strongly dominated by the additive noise, which is still fairly moderate in Figure 5(a-2) [SNR = 12 dB], whereas in Figure 5(a-3) with the SNR = 6 dB (the same as considered in Figure 4), the effect of noise dominates. As seen, the 2D strain maps in Figure 5(b-1), (b-2), and (b-3) show that only in the noiseless case (b-1) is the 25% strain contrast fairly evident, whereas even for moderate SNR = 12 dB the contrast in the strains already becomes somewhat uncertain in the 2D map [Figure 5(b-2)] and almost indistinguishable in individual depth profiles [Figure 5(c-2)]. Finally, for SNR = 6 dB, the strain contrast becomes hardly visible even in the 2D map [Figure 5(b-3)], whereas individual depth profiles become completely corrupted by the noise [Figure 5(c-3)]. This is explained by small magnitude of the phase gradients when subjected to 0.1% strain. We emphasize that for an order of magnitude larger strain = 2% illustrated in Figure 4, the phase gradients are also correspondingly larger, so that even at SNR = 6dB, the hybrid processing with supra-pixel compensation of displacement allows for very clear mapping rather moderate 25% strain contrast [Figure 4(c-2) and (d-2)].

In conventional phase-resolved approaches normally used for strains below $10^{-3}-10^{-4}$ levels, the problem of measuring smaller phase gradients can be addressed by applying averaging procedures. This can be feasible for stable periodic and repeatable tissue deformation (e.g., by a piezo-actuator [20]) using *ex vivo* samples. However, bearing in mind the possibility of manually-produced deformation in the compression elastography, one needs a strain-estimation method which could be reliably applied to a

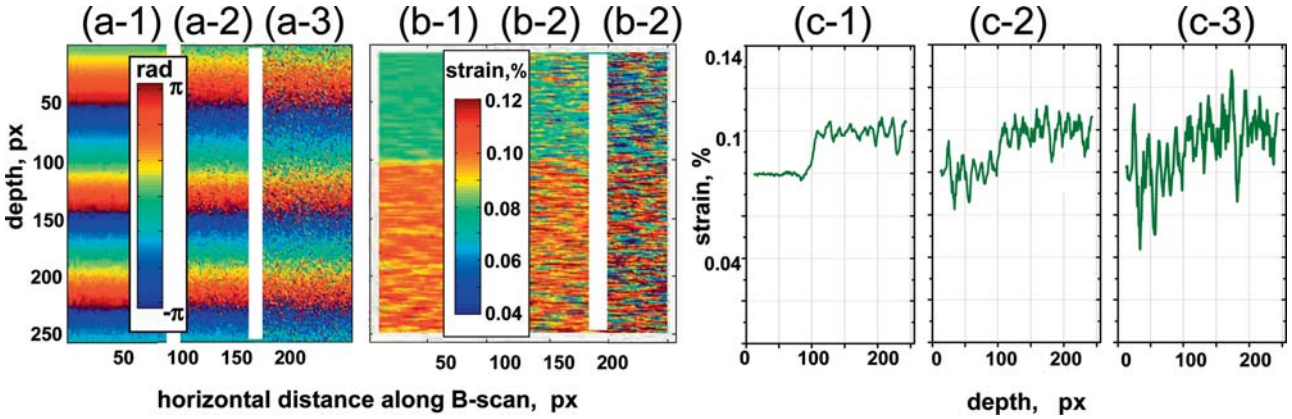

Figure 5 Simulated examples of the strain map reconstruction via phase-gradient fitting for strain 0.1% in the upper layer (an order of magnitude smaller than in Figures 3 and 4). Panels (a-1), (a-2), and (a-3) show the phase difference between the reference and deformed scans found for zero noise, noise levels with SNR = 12 dB, and with SNR = 6 dB, respectively. Slight noise-like fluctuations visible in Figure 5(a-1) are entirely due to weak decorrelation effects, whereas in panels (a-2) and (a-3) phase-variation irregularities are dominated by the additive noise. Panels (b-1), (b-2) and (b-3) show the strain maps for zero additive noise, SNR = 12 dB and SNR = 6 dB, respectively. Panels (c-1), (c-2), and (c-3) show examples of 1D depth profiles of strain taken from 2D plots (b-1), (b-2), and (b-3). Correlation maps are not shown, because the displacements only weakly reduce cross-correlation between the compared images, so that cross-correlation coefficient Ccorr remains ~ 0.9 (in the absence of noise), $C_{corr} \sim 0.85$ (for SNR = 12 dB), and $C_{corr} \sim 0.7$ (for SNR = 6 dB) over the entire scan area, but despite fairly high correlation [cf Figure 4(b-2)], the strain inhomogeneity becomes almost indistinguishable in the presence of noise because of an order of magnitude smaller phase gradient than in Figure 4.

single pair of compared OCT scans. In the HPRDT method, the necessary high tolerance to noises illustrated in Figure 4 for SNR = 6 dB is ensured by allowable fairly large strains ~1.5–2% or even greater (limited by the onset of intense speckle blinking depending on the scanner spectral width) and correspondingly larger strain-induced phase gradients.

Furthermore, Figure 6 illustrates that unlike strains ~0.1%, for which SNR = 6–12 dB already strongly masks the 25% stiffness contrast [see Figure 5], for an order of magnitude larger strains ~1% even for SNR = 0 dB (i.e., signal level = noise level) and the same other parameters, the HPRDT method of phase-resolved processing combined with supra-pixel displacement compensation yields strain map [Figure 6(a-3)] with well-visible 25% strain contrast and quality comparable with that for SNR = 6 dB [Figure 6(a-2)]. The size of the processing window in Figure 6 is 16 px × 16 px, i.e., only slightly greater than 10 px × 16 px in Figures 3, 4, and 5. For comparison Figures 6(b-1) and 6(b-2) also show strain maps obtained via application of the correlational speckle-tracking technique with the same window size and sub-pixel displacement accuracy that, in the absence of other noises, is limited exclusively by strain-induced speckle blinking and can reach $10^{-2} - 10^{-4}$ px [7]. Strains in Figure 6(b-1) and (b-2) are found by fitting the displacement gradient (by analogy with fitting the phase gradient Figure 6(a-1) and (a-2)). Figure 6(b-1) clearly illustrates that in contrast to HPRDT method based on phase measurements, the correlational tracking yields only a very uncertain reconstruction of the 25% stiffness difference even in the absence of additive noise (exclusively because of masking strain-induced decorrelation); and for SNR = 6 dB, the strain map becomes completely corrupted. Reducing strain does not help to improve the accuracy of the correlational tracking since masking decorrelation and measured displacement both are proportional to strain, as discussed in detail in [7]. In this context, increased robustness to strain-induced decorrelation [15] and tolerance to additive noises become very important practical advantages of the HPRDT method.

The proposed method was experimentally tested in the conditions close to its planned free-hand operation, as schematically illustrated in Figure 7 and showing how the output window of the OCT probe produces deformation of the studied sample. A series of several tens of B-scans were recorded; during data collection, 2–3 cycles of loading/unloading of the sample were manually produced, allowable probe displacement being in the range of several % strain amplitude. From the resultant data set, a pair of B-frames corresponding to approximately ~1% strain was selected for subsequent strain mapping by the HPRDT method. In future, the procedure of strain estimate over the entire depth and selection of suitable frames for analysis will be automated.

Figure 8 demonstrates the experimental application of the HPRDT method for mapping strain distribution in a three-layer phantom made of rigid semi-transparent plastic layer I and two layers II and III of deformable silicone, with layer III being ~3X

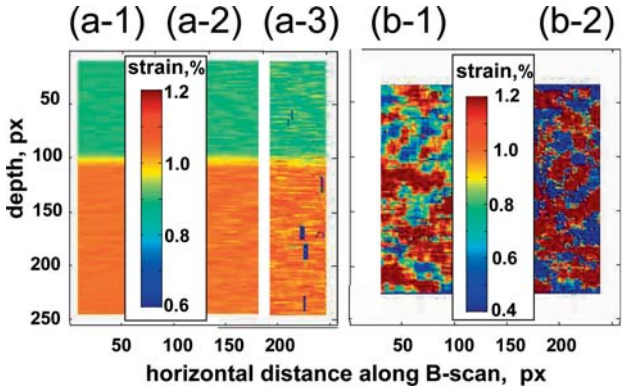

Figure 6 Simulated illustration of high robustness of HPRDT method with respect to additive noise. Strain in the lower softer layer is 1% producing noticeable speckle blinking, so that in the absence of other noises the average cross-correlation between the compared scans drops down to $C_{corr} \sim 0.6$. The window size is 16 px × 16 px (i.e. comparable with 16 px × 16 px in Figures 3 through 5). Panel (a-1) is the reconstructed strain map for zero additive noise, (a-2) is for strong noise with SNR = 6 dB, and (a-3) is for very high noise with SNR = 0 dB (signal level = noise level), for which cross-correlation drops down to $C_{corr} \sim 0.1$. Even for SNR = 0 dB, due to allowable higher strains and phase gradients, the HPRDT method makes it possible to fairly well visualize the 25% stiffness difference. Panels (b-1) and (b-2) show similar strain maps found by fitting displacement gradients obtained using correlational speckle tracking for the noiseless case and SNR = 6dB, respectively. As seen from panel (b-1), the stiffness contrast is hardly discernable even in the absence of additive noise and is completely masked in the presence of noise in panel (b-2) (cf panel (a-3) obtained by HPRDT method for SNR = 0 dB).

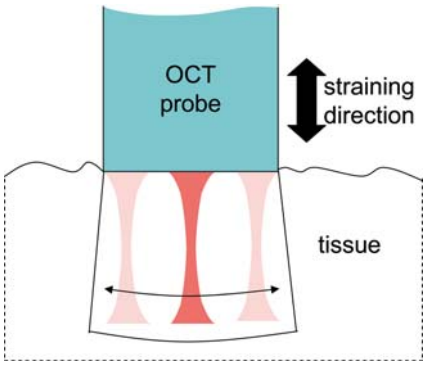

Figure 7 Schematic of the experimental procedure. The diameter of the probe was 6 mm. Characteristic strain, which is the key parameter determining the operability of the method, rather than pressure or force, was approximately controlled.

stiffer than layer II. The three-layer sample is manually compressed from above as discussed above. Figure 8(b) shows that the phase variation remains nearly uniform in the vertical direction within the upper rigid plastic, whereas the two silicone layers clearly show different phase gradients corresponding to displacements of scatterers significantly exceeding the wavelength. The cross-correlation map Figure 8(c) shows that top layer I maintains high correlation due to its rigidity; the softer layer II with transparency similar to that of layer I has significantly reduced cross-correlation coefficient due to both stronger deformation (that causes speckle blinking); and the higher contribution of additive noise in comparison with the stronger scattering and stiffer bottom layer III. Figure 8(d) shows the resultant strain map in which all three layers are clearly seen (the upper one with strain close to zero, the middle softer layer with strain ∼0.5% and the stiffer bottom layer with about 3 times smaller strain. Notice that despite high transparently of the upper layers I and II and strong signal decay in the lower part of layer III, the close-to-zero strain within layer I and step-wise inhomogeneous strain distribution in the underneath layers are surprisingly well reconstructed.

Finally, Figure 9 shows an *ex vivo* example for mucous tissue freshly excised during a gynecological operation for histological examination with structur-

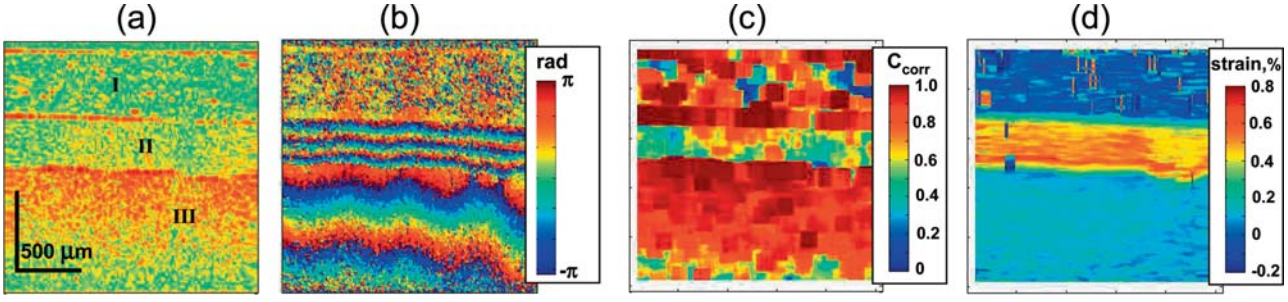

Figure 8 Example of experimental strain map reconstruction under manual compression. The phantom is composed of an almost transparent upper layer of very stiff plastic (I), softer silicon layer with somewhat greater density of scatterers (II), and underneath stronger scattering and ∼3 times stiffer silicone layer (III) at depth. Panel (**a**) is the raw OCT image, (**b**) is the phase-variation map for the compared B-scans, (**c**) is the cross-correlation, and (**d**) is the 2D strain map obtained using the HPRDT method. The ability of the HRDT method to operate under low SNR makes it possible to rather reliably reconstruct close-to-zero strain in the rigid and transparent upper layer (I) despite the very weak scattering.

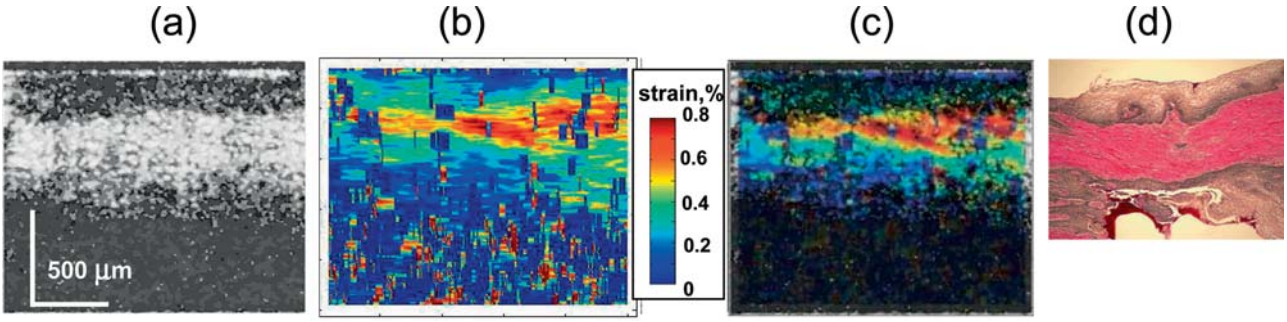

Figure 9 Example of strain map reconstruction via free-hand operation for an *ex vivo* sample of mucous tissue freshly excised during a gynecological operation. Plot (**a**) is a gray-scale structural image, (**b**) elastographic strain map exhibiting a clear 3-layer structure that is superposed with the structural image in panel (**c**), where the semi-transparent color palette slightly differ from (**b**). Panel (**d**) is histological image confirming the presence of three layers (epidermis layers both above and below the central tissue layer that is expected to be softer). The resultant contrast in stiffness appears to be ~2–2.5 times.

al image (a), resultant elastographic map (b), where a 3-layer structure with a softer intermediate layer (with a contrast ~2–2.5X) is clearly seen, superposed structural and elastographic maps (c), and histological image (d). The tissue sample was pinched off such that the epidermal stiffer layers surround the central softer tissue from both top and bottom sides, which agrees well with the elastographically revealed 3-layer sample structure. We emphasize that both Figures 8 and 9 are obtained from a single pair of the compared scans which were acquired under manually-produced compression of the samples by the OCT probe. Conventionally required averaging of multiple scans (which HPRDT obviates) would necessitate stable periodic deformation synchronized with B-scan rate, which is not easily realizable under practical and clinically-relevant free-hand operation.

4. Conclusion

The proposed hybrid method of strain mapping in OCT combines advantages of conventionally used (i) phase-resolved measurements of displacements at a sub-wavelength scale and (ii) displacement tracking at the pixel-size scale, the latter scale being more typical of correlational speckle tracking. The displacement range measured by conventional phase methods is significantly restricted by the problem of phase wrapping (that occurs in OCT for displacements $>\lambda_0/2$) and by significant corruption of the phase-measurement accuracy induced by displacements on the order of pixel-scale or greater. Compared to phase methods, correlational displacement tracking potentially allows for measuring larger displacements, but the accuracy of correlational tracking is significantly degraded by the additive and decorrelation noises caused by speckle blinking. Another point in this context is that correlational speckle tracking can potentially estimate not only axial, but lateral displacements as well; however, realization of this advantage of digital image correlation in OCT is challenging and requires application of super-broadband OCT scanners as discussed in detail in [7].

In the HPRDT hybrid method proposed here, the phase unwrapping is either fully unnecessary or at least can be strongly simplified since determining the entire displacements of scatterers is not necessary. Strain is estimated locally over a chosen spatial scale Δz, which is typically much smaller than the entire imaging depth. Consequently, the accuracy of the deduced phase gradients can be ensured over this smaller scale. If necessary, the "local" (inside the chosen window) phase unwrapping can be also performed, both being much easier and without accumulation of eventual errors as compared to conventional methods that typically try to analyze/correct the phase over the entire imaging depth.

Next, adding strains found for smaller depths, absolute displacements can be cumulatively summed up to scales exceeding pixel size. Such displacement tracking makes it possible to introduce the corresponding correction by an integer number of pixels when estimating the phase variation, which significantly improves the measurement accuracy since the proposed tracking method efficiently eliminates the corruption of phase measurements in the range of significant displacements (i.e. significantly greater than several wavelengths and even larger than the pixel scale), a problem that plagues conventional phase-resolved approaches. Thus, the measurable range of strains can be extended up to levels of a few per cent, for which pronounced speckle blinking and displacement-induced decorrelation already occur, so that conventional correlational speckle tracking techniques and conventional phase-resolved methods become practically inoperable. In contrast, the strongly extended ranges of HPRDT's measurable displacements, strains and resultant phase gra-

dients confer significant tolerance of the HPRDT method to additive noises, thus enabling accurate strain recovery even under these very challenging conditions. This is especially favorable for hand-held operation, for which it is nearly impossible to create controllable periodic deformations and suppress noises by averaging many periods.

Finally, we emphasize that unlike most conventional methods of finding strains, the initial determination of displacements is not necessary in the proposed HPRDT approach. In contrast, we use locally estimated strains for subsequent estimation of accumulated displacements, and the latter are in turn used for enhancing the accuracy of strain estimation in regions where absolute displacements can reach several pixels. Therefore, the proposed hybrid approach is not a straightforward combination of phase-resolved and conventional correlational-tracking methods. The performed simulations and experimental feasibility tests demonstrate promising tolerance of HPRDT method to additive noises, strain-induced speckle blinking, as well as displacement-induced decorrelation. From the viewpoint of computational costs, the proposed approach is much less demanding than correlational speckle tracking and is quite comparable to conventional phase-resolved signal processing. In light of these many potential advantages, practical *in vivo* OCE implementation in the clinic may also be enabled.

Acknowledgements Development of elastographic algorithms and their numerical verification was supported by the RFBR grant No 13-02-00627 and partially by the contract No 02.B49.21.0003 between the Russian Ministry of Education and Nizhny Novgorod State University. The design of the OCT scanner used in this study was funded through the RF Government contract 14.B25.31.0015. Experimental testing of the developed approach was supported by the RSF grant No 14-15-00538.

References

[1] J. Schmitt, Opt. express **3**, 199–211 (1998).
[2] J. Rogowska, N. A. Patel, J. G. Fujimoto, and M. E. Brezinski, Heart **90**, 556–562 (2004).
[3] J. Rogowska, N. Patel, S. Plummer, and M. E. Brezinski, The British Journal of Radiology **79**, 707–711 (2006).
[4] C. Sun, B. Standish, and V. X. D. Yang, J. Biomed. Opt. **16**, 043001 (2011).
[5] A. Nahas, M. Bauer, S. Roux, and A. C. Boccara, Biomed. Opt. Expr. **4**, 2138 (2013).
[6] C. Sun and B. Standish, J. Biomed. Opt. **18**(1–9), 121515 (2013).
[7] V. Y. Zaitsev, A. L. Matveyev, L. A. Matveev, G. V. Gelikonov, V. M. Gelikonov, and A. Vitkin, J. Biomed. Opt. **20**(1–12), 75006 (2015).
[8] J. Fu, F. Pierron, and P. D. Ruiz, J. Biomed. Opt. **18**(12), 121512 (2013).
[9] R. K. Wang, S. Kirkpatrick, and M. Hinds, Appl. Phys. Lett. **90**(1–4), 164105 (2007).
[10] B. F. Kennedy, S. H. Koh, R. A. McLaughlin, K. M. Kennedy, P. R. T. Munro, and D. D. Sampson, Biomed. Opt. Express **3**, 1865–1879 (2012).
[11] V. Y. Zaitsev, L. A. Matveev, G. V. Gelikonov, A. L. Matveyev, and V. M. Gelikonov, Laser Phys. Lett. **10**(1–5), 065601 (2013).
[12] V. Y. Zaitsev, L. A. Matveev, A. L. Matveyev, G. V. Gelikonov, and V. M. Gelikonov, J. Biomed. Opt. **19**(1–12), 21107 (2014).
[13] S. Wang, K. V. Larin, J. Li, S. Vantipalli, R. K. Manapuram, S. Aglyamov, S. Emelianov, and M. D. Twa, Laser Phys. Lett. **10**(1–6), 075605 (2013).
[14] V. Y. Zaitsev, V. M. Gelikonov, L. A. Matveev, G. V. Gelikonov, A. L. Matveyev, P. A. Shilyagin, and I. A. Vitkin, Radiophys. Quant. Electron. **57**, 52–66 (2014).
[15] V. Y. Zaitsev, I. A. Vitkin, L. A. Matveev, V. M. Gelikonov, A. L. Matveyev, and G. V. Gelikonov, Radiophys. Quant. Electron. **57**, 210–225 (2014).
[16] L. Chin, A. Curatolo, B. F. Kennedy, B. J. Doyle, P. R. T. Munro, R. A. McLaughlin, and D. D. Sampson, Biomed. Opt. Express **5**(1–18), 2913 (2014).
[17] B. F. Kennedy, K. M. Kennedy, and D. D. Sampson, IEEE J. Selected Topics in Quant. Electron. **20**(1–17), 7101217 (2014).
[18] T. Marvdashti, L. Duan, K. L. Lurie, G. T. Smith, and A. K. Ellerbee, Opt. Lett. **39**, 5507–5510 (2014).
[19] D. C. Ghiglia and M. D. Pritt, Two-Dimensional Phase Unwrapping: Theory, Algorithms, and Software (Wiley, New York, 1998).
[20] G. Guan, C. Li, Y. Ling, Y. Yang, J. B. Vorstius, R. P. Keatch, R. K. Wang, and Z. Huang, J. Biomed. Opt. **18**(1–7), 111417 (2013).
[21] C. Kasai, K. Namekawa, A. Koyano, and R. Omoto, IEEE Trans. Sonics Ultrasonics **32**, 458 (1985).
[22] V. Y. Zaitsev, L. Matveev, A. L. Matveyev, G. V. Gelikonov, and V. M. Gelikonov, Laser Phys. Lett. **11**, 105601 (2014).
[23] J. S. Bendat and A. G. Piersol, Random Data: Analysis and Measurement Procedures (New York: Wiley, 1986).